Journal of Advanced Joining Processes 11 (2025) 100312

Contents lists available at ScienceDirect

Journal of Advanced Joining Processes

journal homepage: www.sciencedirect.com/journal/journal-of-advanced-joining-processes

Heat treatment optimisation of 18 % Ni maraging steel produced by DED-ARC for enhancing mechanical properties

Maja Lindič [a], Damjan Klobčar [a,*], Aleš Nagode [b], Nikolaj Mole [a], Borut Žužek [c], Tomaž Vuherer [d]

[a] Faculty of Mechanical Engineering, University of Ljubljana, Aškerčeva cesta 6, 1000 Ljubljana, Slovenia
[b] Faculty of Natural Sciences and Engineering, University of Ljubljana, Aškerčeva cesta 12, 1000 Ljubljana, Slovenia
[c] Institute of Metals and Technology, Lepi pot 11, 1000 Ljubljana, Slovenia
[d] Faculty of Mechanical Engineering, University of Maribor, Smetanova ulica 17, 2000 Maribor, Slovenia

ARTICLE INFO

Keywords:
DED-ARC
GMAW
Maraging steel
Heat treatment
Material properties optimisation
RSM

ABSTRACT

This article deals with the Directed Energy Deposition using Wire and Arc (DED-ARC) for maraging steel cladding. A technology for cladding using Gas Metal Arc Welding (GMAW) has been developed that enables the perfect deposition of maraging steel. The material characterisation was carried out in different material states: in the as-built, solution annealed and aged. The research included visual examinations, optical microscopy, Scanning Electron Microscopy / Energy-dispersive X-ray spectroscopy (SEM/EDS), fractography, hardness testing, tensile testing and impact toughness testing. The as-deposited state exhibited a microstructure with very long crystal grains and microsegregations orientated the direction of the heat sink, consisting of lath martensite. Consequently, a subsequent heat treatment is absolutely necessary in order to obtain a uniform fine-grained microstructure. Two different solution annealing processes were analysed, which allowed us to select the most suitable process for the first step of heat treatment followed by aging. A response surface methodology was used to optimise the aging conditions. The results show that additively manufactured maraging steel reaches a tensile strength of 1947 MPa, a hardness of 657 HV5 and a Charpy impact toughness of 11 J at peak aging condition, which is comparable to conventionally manufactured maraging steel.

Introduction

Maraging steels are special types of ultra-high strength steels, in which the high strength is the result of precipitation hardening through the formation of intermetallic compounds coupled with a martensitic transformation. There is no carbon-induced strengthening mechanism typical of conventional steels (ASM International, 2009). Due to their excellent mechanical properties, weldability and the fact that they do not need to be preheated, they are often used as the hot working tools e. g., die stamps, extrusion tools, die-casting moulds and plastic moulds, overlays at hot-shear blades (Schweissmaterialien GmbH, 2024). Maraging steels can be welded by Gas Tungsten Arc Welding (GTAW), plasma and Gas Metal Arc Welding (GMAW). There are some recommendations for welding that should be followed: it should be welded with low heat input (< 1.8 kJ/mm (Kage et al., 1992)), maintaining a low interpass temperature (< 120 °C) and longer periods at elevated temperature and slow cooling rates should be avoided. High heat input leads to a large bead size which cause the formation of a coarser, segregated microstructure with low strength and impact toughness (Lang and Kenyon, 2021).

The use of maraging steel in additive manufacturing (AM) processes has been quite well researched. Most studies refer to the laser powder bed fusion (PBF-LB) and laser-directed energy deposition (DED-LB) processes, which are mainly used in AM processes for (18 % Ni) maraging steel (Guo et al., 2022).

Direct energy deposition-arc (DED-ARC or WAAM as Wire Arc Additive Manufacturing) of maraging steel is a complex process in which the material is subjected to multiple thermal cycles and heat accumulation during the deposition process due to the high heat input in each layer. However, there are only a few studies that have investigated maraging steel deposited by DED-ARC using GMAW technology. The existing studies mainly focus on the: optimization of the deposition process (Yang et al., 2022; Xu et al., 2019), the characterization of the microstructure (Yang et al., 2021; Xu et al., 2022), the investigation of

* Corresponding author at: Laboratory for Welding, Faculty of Mechanical Engineering, University of Ljubljana
E-mail address: damjan.klobcar@fs.uni-lj.si (D. Klobčar).

https://doi.org/10.1016/j.jajp.2025.100312

Available online 16 May 2025

the mechanical behaviour (Yang et al., 2021) and the heat treatment processes (Xu et al., 2018).

As a consequence of DED-ARC manufacturing process the material undergoes multiple heat treatment cycles during the deposition process. This leads to several effects: prior austenite grain (PAGs)/block refinement, and precipitation hardening, which lead to material strengthening and tempering, resulting in material softening (Xu et al., 2022). The grain boundary structure of DED-ARC deposited components in as-built condition is typically dendritic/columnar, similar to the same material deposited by Selective Laser Melting (SLM) (Xu et al., 2019). Low angle grain boundaries (LAGB) structure, segregation and thermal straining are characteristic for such material (Xu et al., 2018).

Various thermomechanical techniques can be used to improve the mechanical properties, such as rolling, which causes plastic deformation of the material and consequently improve the material's response to precipitation hardening, i.e. aging (Xu et al., 2019) or heat treatment processes, where the selection of suitable processes is the key to achieving a sufficient effect on the material properties (Xu et al., 2018).

The heat treatment procedure for maraging steel usually consists of solution annealing and aging step. The procedure largely depends on the chemical composition and manufacturing conditions of the material.

In the case of deposition using DED-ARC, the welding parameters and also other process parameters influence the material in as-built condition. If the heat input during welding is sufficiently low, the microstructure is much less affected by the manufacturing process, and it is not even absolutely necessary to perform a solution annealing step. Therefore, the material can be aged immediately after deposition (Kage et al., 1992). Conversely, welding with high energy input creates similar conditions to casting due to the low cooling rate, which makes solution annealing necessary (Xu et al., 2019).

There are therefore two types of heat treatment processes for the manufacturing condition (i) casting material and (ii) wrought material.

Solution annealing for wrought material takes place at 815–950 °C for 1 h. Heat treatment of large parts (e.g. die-casting dies tools) can be very expensive, so often only precipitation hardening at a temperature around 480 °C for 4 h is performed (Murthy et al., 2019; Qu and Cherkaoui, 2006).

Solution annealing for cast material requires two pre-steps before solution annealing. Preheating to 1150 °C for 1 h to homogenize the material followed by air cooling. The material is then heated to 595 °C for 1 h and then air cooled again to form reverted austenite, which provide nucleation sites during solution annealing. Solution annealing is usually carried out under the same conditions as for the wrought material condition. During this phase, the material is heated significantly above austenite finish temperature. The duration should be sufficient to dissolve the alloying elements into a solid solution. The material is then cooled to room temperature in air (Kage et al., 1992; Kozamernik et al., 2020).

Xu et al. (2018) reported on the correlation between grain structure in as-built condition and heat treatment performance, which is related to the influence on the mechanical properties. They found that for equiaxed high angle grain boundary (HAGB) microstructure, it is sufficient to do the heat treatment for the maraging steel in the wrought condition. Such procedure is not optimal for the dendritic LAGB microstructure, which is characteristic of DED-ARC components.

The correlation between the heat treatment conditions and the mechanical properties is a non-linear problem, which makes it difficult to determine the optimal heat treatment conditions. This requires the use of various statistical methods for data analysis. There are already several studies that use these methods to optimise heat treatment processes. Response surface methodology (RSM) is often used to analyse the influence of heat treatment parameters on mechanical properties (Ray et al., 2003; Zhang et al., 2017; Nunes et al., 2018). Other approaches, such as neural networks and genetic algorithms (Liu et al., 2017; Powar and Date, 2015; Song and Zhang, 2001; Razavi et al., 2016) as well as other statistical modelling techniques (Chen et al., 2024; Adzor et al., 2022; Frihat, 2015; Ščetinec et al., 2023) have also been used.

For a holistic view of the effects of heat treatment, we must therefore consider a wide range of mechanical properties in order to determine the optimum conditions. In the present research, a systematic experimental investigation was carried out using established design of experiments (DoE) methods. The aim of this study was to determine the optimum heat treatment procedure for GMAW DED-ARC deposited maraging steel based on the required mechanical properties.

First, simple geometries–wall structures were produced using DED-ARC, from which specimens were prepared for further analysis. Two different solution annealing procedures were then carried out. The procedure that provided the best results was used as the basis for the subsequent heat treatment of precipitation hardening. The precipitation hardening was carried out under different heat treatment conditions. The results of the mechanical properties after aging were used as input data to DoE model. In this paper, a methodology was applied to investigate the effects of precipitation hardening heat treatment conditions on the mechanical properties.

Regression analysis was a further step beyond DoE and focused on constructing a mathematical model (response surface) that describes the response of the output factors in relation to the input variables. It was used for the multiobjective optimisation of the aging procedure. The mechanical properties were fitted as response surfaces to develop approximation functions for each of the output variable.

A multi-objective analysis of the aging conditions was performed to determine the precipitation hardening parameters that can achieve the required mechanical properties tailored to the specific applications of this material type. This approach allows the identification of the most suitable aging conditions and ensures that the material meets the mechanical performance requirements dictated by the intended application, for instance in the tooling industry. Although the models were developed specifically for maraging steel deposited by the DED-ARC process, the precipitation hardening models presented here are broadly applicable to this class of maraging steels and are not restricted to the DED-ARC method. Furthermore, the solution annealing heat treatment (SA2) developed in this study can also be universally applied to enhance microstructural homogeneity by refining large grains and mitigating non-uniformities.

Materials and methods

Materials and deposition process

An E 4-UM-40 PT welding wire (Capilla 2709 MAG) with a diameter of 1.2 mm was deposited on a X2NiCoMo18-9-5 (BÖHLERW720VMR) base material. The chemical compositions of both materials are shown in Table 1.

A Fronius Trans Pulse Synergic 3200 GMAW power source with the ABB IRB 140 welding robot was used for the experimental DED-ARC of the sample walls. The system is shown in Fig. 1a.

Tailored DED-ARC process parameters are crucial for achieving high-quality deposition. The application of the general guidelines for gas metal arc welding of maraging steels (Lang and Kenyon, 2021) led to deposits with metallurgical defects such as porosity, lack of fusion and cracks due to insufficient heat input and non-optimal interpass temperature. These experiments were performed using the developed Fronius Cold Metal Transfer combined with pulse (CMT + pulse) welding program consisted of 1 CMT and 9 pulse cycles. The following welding parameters were used: welding current 200 A, travel speed 3 mm/s, interpass temperature 250 °C. A shielding gas mixture of 50 % Ar, 50 % He with a gas flow of 15 l/min was used. Each layer was cleaned with a stainless-steel wire brush to remove slag prior deposition of the next layer. We produced several simple multilayer structures with approx. dimension of 180 mm length, 14 mm in width and varying heights ranging from 70 – 120 mm as shown in Fig. 1b.

Table 1
Chemical composition base and filler material [wt.%].

	Ni	Co	Mo	Mn	Si	C	Ti	Al	Fe
Welding wire (Schweissmaterialien GmbH, 2024)	17–19	10–12	4–4.5	<0.3	<0.8	<0.03	+	+	bal.
Base material (voestalpine BÖHLER Edelstahl GmbH and Co KG, n.d.)	18.5	9.0	5.0	≤0.1	≤0.1	<0.03	0.7	0.1	bal.

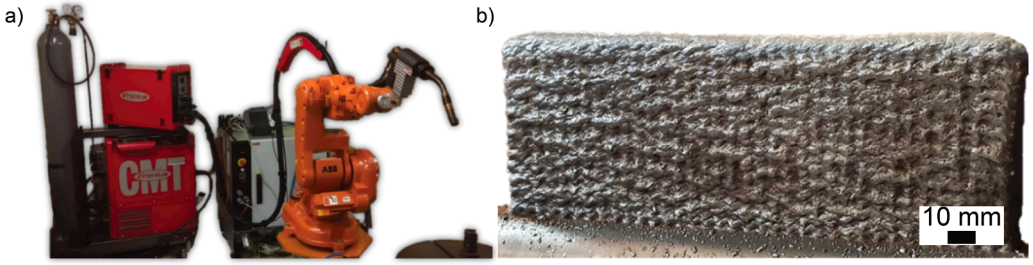

Fig. 1. a) DED-ARC deposition system b) Deposited wall structure.

Heat treatment

The deposited materials were tested both the as-built condition and after heat treatment. The heat treatment consisted of 2 steps: solution annealing and precipitation hardening. The heat treatment was carried out in an air atmosphere according to the schemes presented in Fig. 2. After each heat treatment step, the specimens were cooled to room temperature in the air on the fireclay base. Two procedures of solution annealing procedures were investigated, namely SA1 and SA2, both graphically shown in Fig. 2a-b. SA1 consisted of a solution annealing step at 920 °C for 1 h, while SA2 consisted of a homogenisation step (1150 °C for 1 h), a grain refinement step (595 °C for 1 h) and a solution annealing step at 850 °C for 1 h.

Based on the results of the mechanical properties and microstructure tests, we have selected a solution annealing procedure (SA1 or SA2) that will be used as the basis for further investigation of the aging step. The aging heat treatment is very sensitive to the choice of heat treatment parameters and must be carefully selected depending on the application of the material. The response of the material properties to precipitation hardening is non-linear, which only adds to the complexity of determining the heat treatment conditions based on the output mechanical properties and microstructure. Regression analysis was used to determine the selected aging heat treatment procedure.

First, Central Composite Design (CCD) of Response Surface Methodology (RSM) was used, to perform multi-objective optimisation of aging process. Two significant independent variables, i.e. key parameters, were selected: aging temperature (A) and time (B). The range of lower/upper limits defining our process window was determined based on data from the literature (ASM International 2009). The axial points are in the temperature range of 450–510 °C and in the time range of 2–6 h. The center point was set at 480 °C and 4 h. The precipitation hardening conditions are shown in Fig. 2c. The user-defined design points (condition PH4, PH6, PH8) were adopted as common prescribed aging conditions (ASM International, 2009; Schweissmaterialien GmbH, 2024). Three runs were made for each set of parameters.

A multiobjective regression analysis was performed using Cornerstone 8.0 software (Wember, 2012). A multiple regression analysis was used to optimize the precipitation annealing step. Tensile strength, Charpy impact toughness, Vickers hardness and visual assessment of microstructure were used as responses.

In non-linear regression analysis, is assumed that the relation between continuous dependent variable and independent variable is not linear. In general, a third–order model was used in our model. The fit of the predicted values to the measured values is determined by the Goodness of fit criteria: Coefficient of indication R^2, Standard error of the estimate S_e, Mean Absolute Percentage Error - *MAPE* using Eq. (1)-(3) (Armstrong and Collopy, 1992; Weiss, n.d).

$$R^2 = \frac{SS_{regression}}{SS_{total}} = 1 - \frac{SS_{residual}}{SS_{total}} = 1 - \left(\frac{\sum_{i=1}^{n}(\hat{y}_i - \overline{y}_i)^2}{\sum_{i=1}^{n}(y_i - \overline{y}_i)^2}\right) \quad (1)$$

$$S_e = \sqrt{\frac{\sum_{i=1}^{n}(y_i - \hat{y}_i)^2}{n-2}} \quad (2)$$

$$MAPE = \frac{\sum_{i=1}^{n}\left|\frac{y_i - \hat{y}_i}{y_i}\right|}{n} \cdot 100 \quad (3)$$

where y_i - represent the observed/measured value, $\hat{y}_i$ – predicted values and n – number of observations. Validation and accuracy of the model

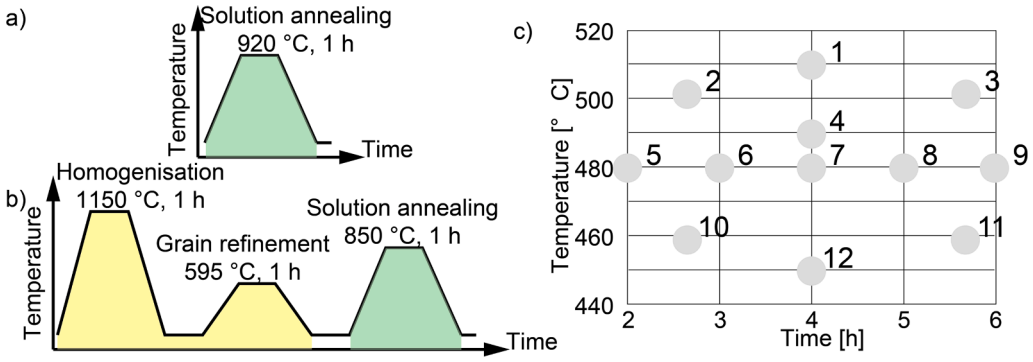

Fig. 2. Investigated solution annealing conditions a) SA1, b) SA2 and c) precipitation hardening conditions - PH.

were determined using the criteria in these equations.

Metallographic analysis and mechanical testing

Various samples were cut from the deposited wall, corresponding to the dimensions required for each test according to the relevant standard. The orientation of the cut samples is shown in Fig. 3a. Metallographic analysis using optical microscopy, SEM and fractography were performed together with mechanical tests such as Charpy tests, Vickers hardness and tensile tests to characterize the influence of the post-processing heat treatment on the deposited maraging steel.

For metallographic analysis, the material was sectioned into samples with dimensions 10 × 10 × 10 mm as shown in Fig. 3a. Each specimen was prepared as follows: mounted in resin, ground, polished and etched with a Kaling 2 solution (100 ml ethanol, 100 ml HCl, 2 mg CuCl2). The Keyence VHX 6000 digital optical microscope and ZEISS CrossBeam 550 Focused Ion Beam Scanning Electron Microscopy (FIB-SEM) microscope was used for metallographic analysis and analysis of fractured surfaces. The chemical composition was examined using Energy-dispersive X-ray spectroscopy (EDS) using Silicon Drift Detector (SDD) Ultim Max 65 m^2 detector (Oxford Instruments).

The Vickers hardness was measured with the Zwick Roell ZHU 2,5 using the Vickers intender at a load of 5 kg in accordance with the EN ISO 6507 standard. Measurements were done on the samples for metallographic analysis three times on each sample.

Instrumented Charpy impact strength was determined according to the EN ISO 148-1 and ASTM E2290-15 standards. Specimens of 10 × 10 × 55 mm with a V-notch were tested using the Amsler Charpy pendulum RPK300.

Tensile specimens with the geometry shown in Fig. 3b were tested according to the ISO 6892-1 - Method B standard on the Instron 8802 servo-hydraulic testing system with an extensometer.

Results and discussion

Microstructure analysis

Micrographs of the samples taken in as-built condition are shown in Fig. 4a-b. Material shows no visible porosities, lack of fusion or other visible defects, indicating a completely dense material of the DED-ARC part in the as-built condition. In the area between two subsequent layers, very long crystal grains with micro-segregations oriented in the direction of the heat sink (1) can be recognised. The remelting line (4) is quite pronounced. Areas with a fine-grained microstructure (2), transitioning to a coarse-grained (3), can also be seen. The different shape and size of the crystal grains is the result of the remelting and solidification, the temperature gradient, the temperature exposure and the cooling rate during the deposition process and the cyclic reheating and/or remelting of each layer. A cellular-dendritic microstructure is formed in the heat-affected zones (HAZ). The microstructure consists of lath martensite. The microstructure is inhomogeneous and varies greatly depending on the location, which can also be confirmed by EDS mapping, as can be seen in Fig. 5.

As shown in Fig. 5, the Mo enriched regions also exhibit higher concentration of Ni and Ti, while the Fe content is relatively low. The average elemental composition of the matrix determined by EDS analysis is as follows: Mo 4 wt. %, Ni 18 wt. %, Co 12 wt. %, Ti 1.5 wt. %, minor amounts of Al and Si <0.2 wt. %, and the balance is Fe at 64 wt. %. Al and Ti are also observed in round formations (see Fig. 5a). Based on the EDS analysis of the inclusions, we found that the average content: Ti 18 wt. %, Al 13 wt. %, and O 32 wt. %, indicating the presence of complex Ti-Al oxides. A similar but less pronounced pattern is seen for Ti and Mo. In these cases, the EDS analysis detects the presence of (Ti, Mo) C as these elements dominate in the chemical composition with an average content: Ti 10 wt. %, Mo 11 wt. %, and C 22 wt. %. However, it should be noted that EDS analysis of carbon in steels is not accurate as carbon has a low atomic number, resulting in a weak X-ray emission that is easily absorbed. In addition, contamination and background noise can interfere with the accurate detection of a carbon.

The microstructure after SA1 treatment (Fig. 4c-d) is more homogeneous compared to the sample in the as-built condition (Fig. 4a-b), although the inhomogeneity is not completely eliminated by SA1 solution annealing. When the sample is heated to the austenitic region, the homogenization process takes place, which is also reflected in the structure after solution annealing. As a result, solution annealing at a higher temperature is more efficient due to the faster diffusion rate. The results are also reflected in the EDS mapping, as can be seen in Fig. 5b The microsegregation is still noticeable, but the elements are more evenly distributed than in the as-built condition. We can conclude that SA1 influences homogenization, but not sufficiently. Homogenization was not fully achieved, which could be due to either insufficient temperature or insufficient duration of the process.

In the case of SA2 (Fig. 4e-f), homogenisation of microstructure was achieved in selected time with the first step, homogenisation annealing, as the material is heated highly into austenitic region. During cooling, it transforms into nickel martensite with low hardness. The second step of the heat treatment, i.e. grain refinement, leads to the formation of reverted austenite, which is distributed in the matrix and acts as nucleation sites, resulting in fine-grained austenite after this heat treatment step. Similar results have also been reported by other authors (voestalpine BÖHLER Edelstahl GmbH and Co KG, 2017). In the third, i.e. solution annealing step, the alloying elements are evenly distributed in the microstructure, as seen on EDS mapping in Fig. 5c. During cooling, a low hardness martensite saturated with alloying elements is formed. In the case of SA2, solution annealing was carried out at a lower temperature than for SA1. Two pre-steps in SA2 have a greater effect on the microstructure than a higher annealing temperature in SA1, which can also be seen from the comparison of Fig. 4c-d and e-f. The microstructure is completely homogeneous and shows no detectable influence of the manufacturing process. This is also crucial for the precipitation hardening of steel, as more evenly distributed precipitates are form after precipitation hardening, leading to better mechanical properties.

Homogeneity of the microstructure highlights the importance of heat treatment. Solution annealing plays a crucial role in reducing inhomogeneity and reduced segregation to achieve more uniform material characteristics. It also influences the size and distribution of the crystal grains, which in turn affects the material's ability to absorb energy and deform plastically without cracking, prevent crack propgation, reduce the likelihood areas of stress concentration, better resist fatigue and reduce the rate of crack initiation and their further propagation (Kage

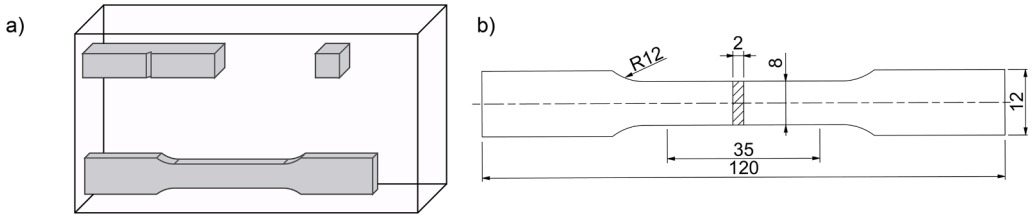

Fig. 3. a) Scheme of samples orientations inside cut from wall, b) tensile specimen dimensions [mm].

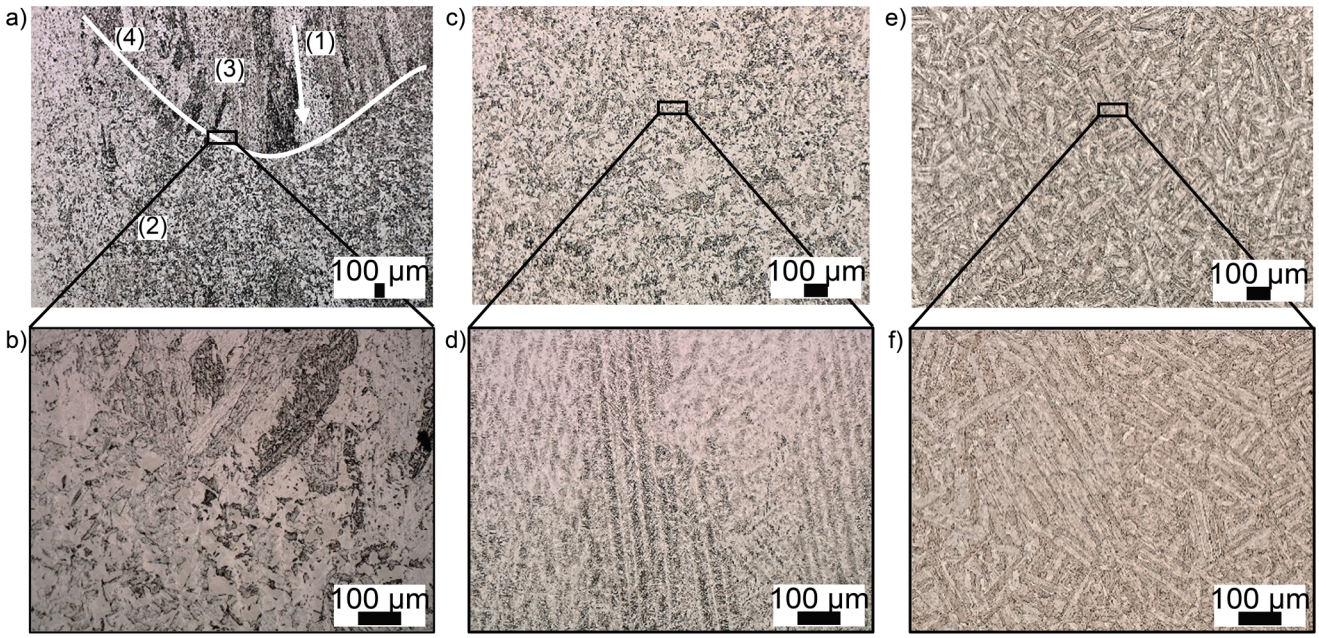

Fig. 4. Optical micrographs at lower and higher magnifications: a), b) in as-built condition c), d) after solution annealing SA1 and e), f) after SA2.

et al., 1992; Qu and Cherkaoui, 2006). A fine-grained and uniform structure has a positive effect on the mechanical properties. From this, we conclude that the SA2 process is more suitable for the initial stage of heat treatment, followed by aging.

The microstructures of all samples from SA2+PH1 to SA2+PH12 were thoroughly analysed. Representative microstructures, shown in Fig. 6a-c were selected for presentation to illustrate the typical behaviour of the material. Representative conditions shown in this article are: under-aged condition SA2+PH10 (aged at 459 °C, 2.6 h), peak-aged condition SA2+PH7 (aged at 480 °C, 4 h) and over-aged condition SA2+PH3 (aged at 501 °C, 5.4 h). The classification of the individual microstructures is shown in Fig. 6e.

In samples SA2+PH2, SA2+PH5, SA2+PH10, SA2+PH11 and SA2+PH12 there are no significant changes in the microstructure after ageing. At these lower temperatures and/or shorter times, precipitation was less pronounced, and the microstructure is under-aged. Typical microstructure is shown in Fig. 6a. The EDS mapping in Fig. 5d reveals a completely uniform distribution of elements throughout the matrix, with no noticeable segregation. The exceptions are the chemical elements Al, and, in some areas, Ti and Mo, which additionally contribute to the formation of inclusions. Shortly after the material has reached the peak-aged condition, the precipitates in the matrix begin to coarsen (voestalpine BÖHLER Edelstahl GmbH and Co KG, 2017). The material begins to overage.

In samples SA2+PH4, SA2+PH6, SA2+PH7, and SA2+PH8, a peak-aged microstructure was observed, which is consistent with the optimal aging conditions described in the literature (ASM International, 2009; Schweissmaterialien GmbH, 2024). The typical microstructure is shown in Fig. 6b. The EDS mapping of chemical elements distribution, shown in Fig. 5e, corresponds to that observed in the under-aged condition.

The samples classified as over-aged are those labelled SA2+PH1, SA2+PH3, and SA2+PH9. The representative microstructure that best illustrates the condition of over-aged samples is SA2+PH3 and is shown in Fig. 6c. Here, the precipitation hardening process is most pronounced, and the microstructure of the material has completely changed, becoming characteristically cellular. In Fig. 6d, sample SA2+PH9 shows a less pronounced over-aged microstructure, where the onset of over-aging and structural changes are visible, but not yet advanced enough to completely change the structure. During over-aging, nickel-molybdenum precipitates (Ni_3Mo) transform into more stable phases of iron-molybdenum precipitates (Fe_2Mo). As the Ni_3Mo precipitates transform, nickel migrates back into the matrix or contributes to the formation of other intermetallic phases, leading to a localised increase in nickel concentration, as shown by the EDS mapping in Fig. 5f. These nickel-rich regions typically occur at the boundaries of martensite laths or near precipitates, as other authors have also found (Jägle et al., 2014). Nickel reduces the temperature of martensite transformation – Ms, as other researchers have found (Carvalho et al., 2019; Liu et al., 2023). If the temperature of the material rises above the local Ms during precipitation hardening due to the nickel-rich regions, this can cause the martensite to transform back into austenite, which is known as reverted austenite. As precipitation hardening process progresses, more and more areas reach the conditions for transformation, so that the amount of reverted austenite increases, as also confirmed by a previous study (Carvalho et al., 2019).

Analysis of microhardness

A summary Table 2 showing the average values of the measured mechanical properties, i.e. Vickers hardness, yield strength, tensile strength, elongation and Charpy impact strength under different conditions. The graph in Fig. 7 shows the measured hardness profiles along the height of the deposited wall for different material conditions: As-built, SA1, SA2, and SA2+Peak aged. The Vickers hardness measurements were taken along the centreline of the wall in a cross-section, with evenly spaced intervals between measurement points. For the as-built and SA1 states, a larger number of measurements were performed as a larger scatter was expected, while for the SA2 and SA2+Peak aged conditions, fewer measurements were performed due to the expected more homogeneous structure.

In the as-built condition, material has an average Vickers hardness of 465 HV5. An inhomogeneous microstructure has a significant effect on the consistency of the mechanical properties and depends strongly on the measurement zone, as also reported by other authors (Jorge et al., 2018). The differences depend on whether the microhardness is measured in the centre of the deposited layer, where the hardness is lower, or in the area close to the fusion line, where the hardness is higher due to the higher heat sink. Similar observations have also been reported by other researchers (Murthy et al., 2019).

In addition, the microhardness varies from the bottom to the top of

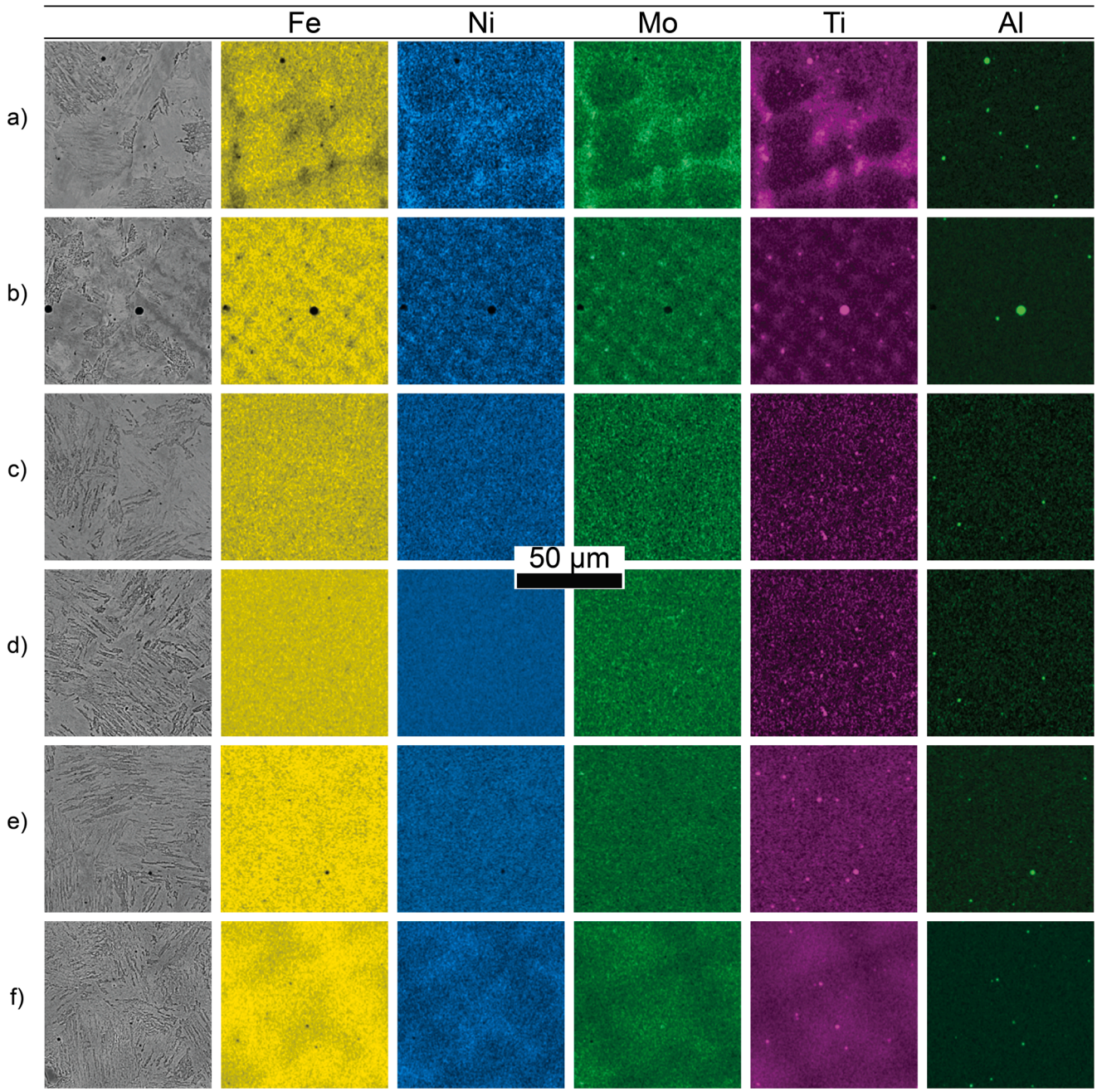

Fig. 5. EDS mapping of several of chemical elements at different material conditions: a) as-built, b) SA1, c) SA2, d) under aged condition SA2+PH10, e) peak aged condition SA2+PH7, f) over aged condition SA2+PH3.

the deposited material. The microhardness near the top of the deposition is lower compared to the material near the base material, which is due to the lack of subsequent thermal cycles, which are causing precipitation hardening of the previously deposited material, as shown in Fig. 6. Other studies have also shown comparable findings (Kozamernik et al., 2020). It is precisely for this reason that the average measured value is outside the Vickers hardness range specified by the wire manufacturer, which is 372-392 HV5 in the as-built condition (Schweissmaterialien GmbH, 2024). This hardness range is only achieved in the upper layers, which were not exposed to thermal cycling.

The first cycle of heat treatment is solution annealing, during which the hardness of the material decreases. As shown in Table 2, the Vickers hardness for SA1 was 331 ± 11 HV5, while the hardness for SA2 was 321 ± 4 HV5. The scatter in the hardness measurements after SA2 is almost three times lower than in the measurements after SA1. This reduction is attributed to the homogenisation of the microstructure, which has a direct effect on the measurement scatter. A more homogeneous microstructure without precipitates, which dissolve during solution annealing, leads to a lower variability of hardness.

During the aging process, the material undergoes an intrinsic heat treatment that stimulates the formation of precipitates, which leads to an increase in hardness. In the under aged conditions this phenomenon is not sufficiently pronounced. Therefore, the Vickers hardness in this condition is measured at 612 HV5 under the condition SA2 + PH10. The hardness of the sample in the under-aged condition is the lowest compared to that in the peak and over-aged conditions. The measured Vickers hardness value for the peak-aged condition (SA2 + PH7) was 657 HV5 and the value for the over-aged condition (SA2 + PH3) was 689 HV5.

The lowest Vickers hardness of all samples is exactly at the condition

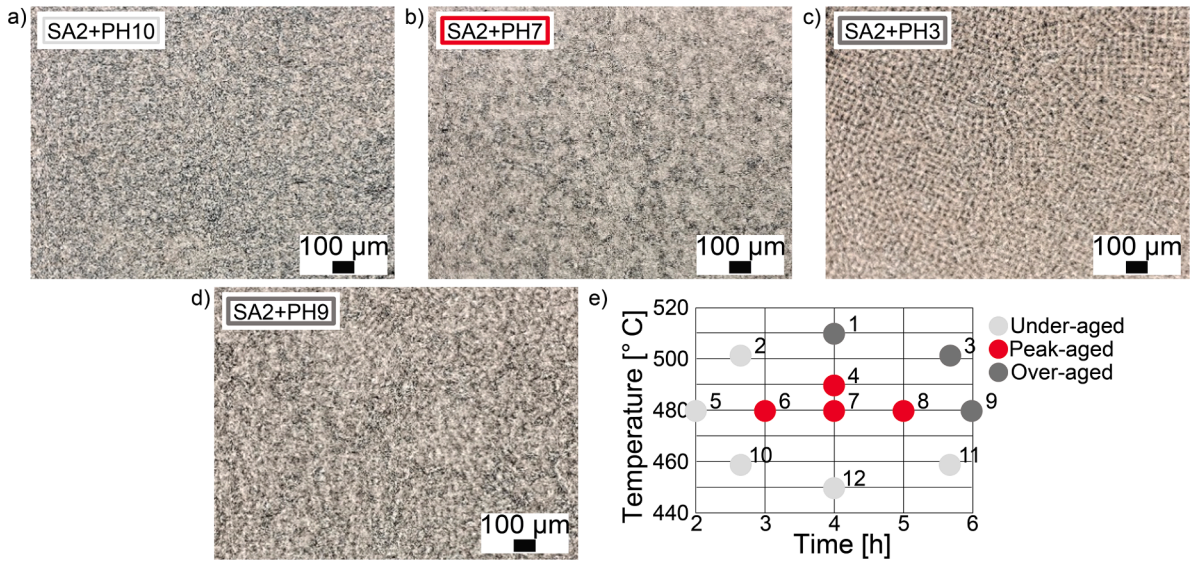

Fig. 6. Representative microstructures after precipitation hardening: a) under aged condition SA2+PH10, b) peak aged condition SA2+PH7, c) over aged condition SA2+PH3, d) less pronounced over-aged condition SA2+PH9 and e) division of SA2+*x* samples according to the microstructure condition.

Table 2
Mechanical properties in as-built conditions, and after different stages of heat treatment.

	Heat treatment condition	Vickers hardness [HV5]	Impact toughness [J]	Yield strength [MPa]	Tensile strength [MPa]	Elongation [%]
as-built	/	465±19	18±2	913±74	1340±100	13.1±0.7
SA1	920 °C, 1 h	331±11	50±2	740±1	1036±1	13.8±0.9
SA2	1150 °C, 1 h; 595 °C, 1 h; 850 °C, 1 h	321±4	43±4	701±7	955±3	9.1±0.9
SA2+PH1	510 °C, 4 h	641±4	14±3	2123±12	2200±16	3.1±0.4
SA2+PH2	501°C, 2.6 h	680±9	10±0	1930±1	1989±9	2.4±0.5
SA2+PH3*	501 °C, 5.4 h	689±1	9±2	1952±15	2016±19	1.9±0.3
SA2+PH4	490°C, 4 h	709±5	11±0	1944±7	2012±1	2.7±0.7
SA2+PH5	480 °C, 2 h	630±1	13±0	1991±19	2079±23	4.2±0.8
SA2+PH6	480°C, 3 h	632±3	12±2	1887±5	1956±6	2.4±0.5
SA2+PH7*	480°C, 4 h	657±3	11±2	1893±3	1947±12	2.0±0.3
SA2+PH8	480°C, 5 h	704±4	11±1	1941±15	2019±14	2.9±0.4
SA2+PH9	480 °C, 6 h	633±17	13±1	1943±2	2012±8	2.9±0.6
SA2+PH10*	459 °C, 2.6 h	612±6	13±2	1725±3	1777±9	1.6±0.1
SA2+PH11	459 °C, 5.4 h	623±2	11±1	1844±11	1918±8	3.2±0.7
SA2+PH12	450 °C, 4 h	619±4	12±1	1904±41	2003±36	2.8±0.2

Under age; Peak age; Over age; *Representative sample of the group

defined as representative (SA2 + PH10), while the maximum hardness value does not fully correspond to with the selected representative condition. The highest hardness was measured at 709 HV5 in the SA2 + PH4 condition. When the material reaches its peak, the precipitates start to coarsen due to Ostwald ripening and reverted austenite can form. All this leads to a decrease in hardness; therefore the hardness is lower in the over-aged condition.

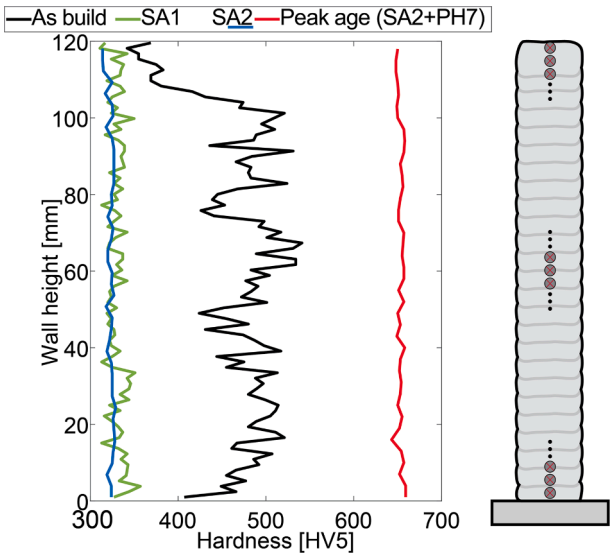

Fig. 7. Vickers hardness profiles along height of deposited material for different material conditions.

Analysis of tensile testing

The results of the average tensile strength tests under various selected material conditions are shown in Table 2. Representative stress-strain diagrams for a randomly selected sample of each material condition are shown in Fig. 8a, while Fig. 8b shows a bar chart of the average values of Vickers hardness, impact strength and elongation. The stress strain curve of the material in the as-built condition has an average tensile strength of 1340 MPa and a high elongation of 13.1 %. The stress-strain curve, shown in Fig. 8a exhibits behaviour that is characteristic of ductile materials.

After solution annealing, the tensile strength decreases and reaches the lowest tensile strength of all conditions. Under condition SA1 the tensile strength is 1036 MPa with an elongation of 13.8 % and under condition SA2 955 MPa with an elongation of 9.1 %. Even under these conditions, the behaviour of the curve is characteristic of ductile materials.

The results of the mechanical properties are shown in Table 2. From the stress-strain curves of the aged samples, it can be seen that the material is on average less ductile in the aged condition but has a higher tensile strength than in the solution-annealed condition. As expected, the tensile strengths of the aged samples are the highest. The tensile strength of the representative under-aged sample (SA2 + PH10) is lower compared to the peak- and over-aged samples, reaching 1777 MPa at an elongation of 1.6 %. The peak-aged sample showed a tensile strength of 1947 MPa at an elongation of 2.0 % under condition SA2 + PH7, while the over-aged sample reached 2016 MPa at an elongation of 1.9 % under condition SA2 + PH3.

The highest tensile strength of all aged samples is achieved by the over-aged sample under the SA2+PH1 condition, which reaches 2200 MPa at an elongation of 3.1 %. The highest tensile strength of the peak-aged samples is slightly lower and is 2012 MPa, at an elongation of 2.7 % under SA2 + PH4.

Analysis of Charpy impact toughness

The results of the impact toughness measurements are shown in Table 2. In addition, we performed a fracture analysis of the fractured surfaces using SEM microscopy and optical microscopy. The fractured surfaces are shown in Fig. 9. Charpy impact toughness in the as-built condition is relatively high at 18 J. This fracture surface shows various sub-areas of dimples, including areas with elongated large dimples (which have formed on inclusions and can therefore grow significantly), shallow dimples (formed by joining of micro voids by shearing along slip bands), and deep dimples, showing the mixed characteristics of a ductile fracture that is also affected by micro-segregation. The structure is consistent with the optical micrographs where a heterogeneous structure was observed due to uneven heat input and cooling.

During solution annealing, the homogeneity of the microstructure increases, and the material becomes softer, which consequently results in an increase in impact toughness, as the following measurements show. The steel after heat treatment SA1 exhibited an impact toughness of 50 J, and after SA2, the Charpy impact toughness was 43 J. The fracture surface of the Charpy impact toughness sample SA1 shown in Fig. 9b exhibits more uniformly distributed dimples compared to the as-built fracture, but several inhomogeneous areas can still be observed. There are many areas of small, shallow dimples, indicating less ductile regions in the material. There are also distinct areas of deeper, highly oriented dimples. The fracture surface after solution annealing SA1 can be described as inhomogeneous. The fracture surface has pronounced shear lips and an arrest area. The fracture surface after solution annealing SA2, shown in Fig. 9d, is completely homogeneous, without the pronounced heterogeneous areas observed in the fracture of SA1. The dimples are round, without characteristic orientation and deep, exhibit the characteristics of a ductile fracture. The impact fracture of specimen shows distinct shear lips and arrest area.

During aging, the precipitation of intermetallic phases increases the material strength, while inversely leading to a reduction in impact toughness. The material in the under-aged condition SA2+PH10

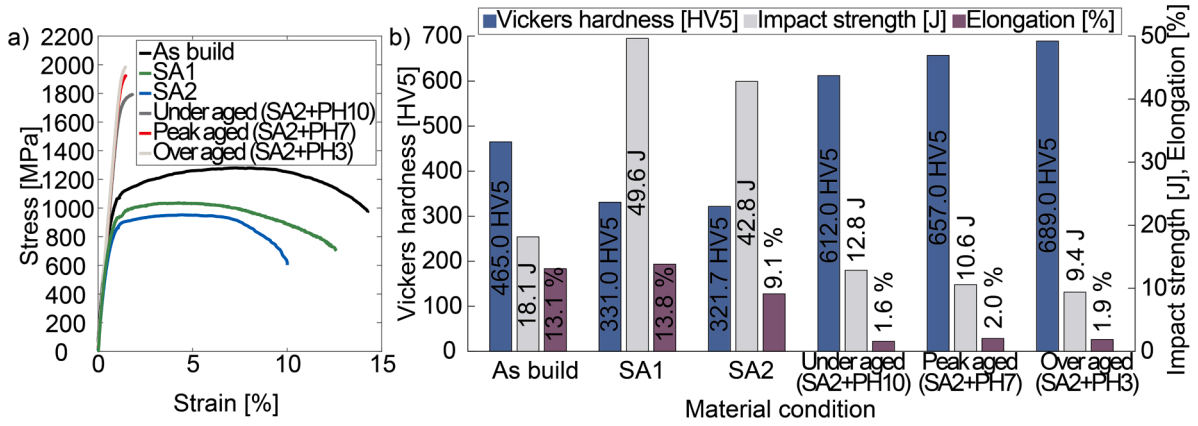

Fig. 8. Diagrams for different material condition a) Stress-strain diagram, b) Average values for Vickers hardness, notched impact strength and elongation in the bar chart.

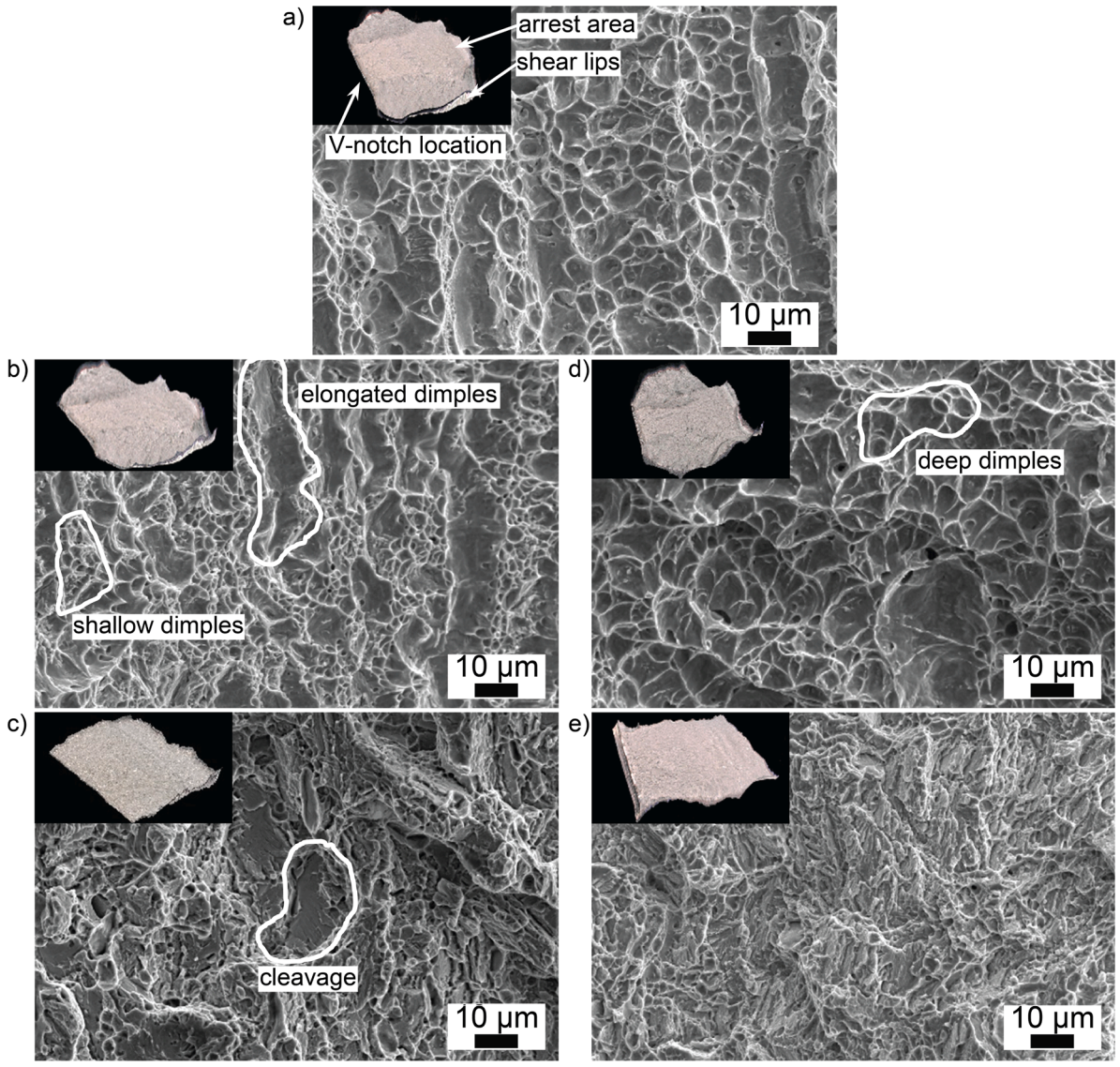

Fig. 9. Fractured surfaces SEM and 3D macrographs of impact test specimens in different conditions: a) as-built, b) SA1, c) SA1+Peak aged, d) SA2 and e) SA2+Peak aged.

condition reaches 11 J and in the over-aged condition SA2+PH3 9 J. The sample at peak-aged condition SA2+PH7 reaches 11 J. The impact toughness decreases with increasing aging temperature or/and time as larger precipitates form, which increases the strength of the steel. Once the material has reached the peak of the precipitation process, the trend reverses as these precipitates begin to coarsen and the steel softens. Over-aging can also lead to a partial reversion of martensite to reverted austenite, which additionally softens the steel, resulting in higher impact toughness (ASM International, 2009).

The response of impact toughness is inversely proportional to the other observed material characteristics, with the global minimum occurring at over-aged condition of SA2 + PH3 and reaching 9 J. The maximum value of impact toughness was measured at 14 J in the over-aged condition of SA2 + PH1.

Although the heat treatment SA1 proved to be an unsuitable basis for further aging, we carried out an additional heat treatment SA1 + peak-aging for comparison with SA2 + peak-aging. The measured value of impact toughness for SA1 + Peak aging was 5 J, which is more than half of the value we obtained when testing SA2 + Peak aging, where we measured 11 J. The fracture surface of SA1 + Peak aging, shown in Fig. 9c, shows inhomogeneous areas. It consists of small and shallow dimples along with inter-lath cleavage regions. However, some large cleavage facets with some secondary cracks can also be observed, indicating regions of high brittleness. Overall, cleavage is the dominant fracture mechanism in this sample.

On the other hand, the fracture surface of SA2 + Peak aging, which can be seen in Fig. 9e, has very few small and shallow dimples. However, it does not exhibit large cleavage facets but shows predominantly inter-lath cleavage with secondary cracks. The predominant fracture mechanism can also be attributed to cleavage.

The fracture surfaces of both aged samples, shown in Fig. 9c and e appear fairly flat with small and indistinct shear lips. The samples show only indicated arrest areas, which is characteristic of brittle materials.

Regression analysis

As part of the application of the multi-objective regression analysis, we first defined the input (independent) and output (dependent) variables of the regression model. The input process variables are heat treatment time [h] and temperature [°C], which are the key parameters of the precipitation hardening process. Based on these input parameters, models were developed to predict three output variables: hardness

[HV], notched impact toughness [J] and tensile strength [MPa]. The models developed are only applicable within the specified international system of units (SI).

The measured data of various mechanical properties were used as input data for the regression analysis model. In order to compare the Goodness of fit parameters, the coefficient of determination - R^2, the standard error of estimate - S_e and the mean absolute percent error - *MAPE* values were calculated. They are shown in Table 3. These data determine how well the model describes the actual response of the system.

The coefficient of determination R^2, is a parameter that characterises the fit of the regression model to the data and ranges from 0 to 1. A higher R^2 value indicates a better fit of the model, with smaller residuals also indicating a better fit. All R^2 values > 0.9 indicate a good fit of the model. In this study R^2 was 0.972 for tensile strength, which means that 97.2 % of the experimental data matched the data predicted data by the model. The model could not explain 2.8 % of the total variation, indicating its adequacy. For Charpy impact toughness the fitting is 93.4 % and for Vickers hardness 95.2 %.

The S_e error is calculated as the square root of the average of the squares of the differences between the predicted and the actual – measured response values. It provides a measure of the accuracy of the model. The deviation from the mean is squared and then the square root of this value is calculated, this measure gives greater weight to larger errors. This means that large errors, i.e. large deviations from the average, have a greater influence on the S_e error than small deviations. The S_e value for the tensile strength is 48.15 MPa, the Charpy impact toughness is 2.133 J, and the Vickers hardness is 23.86 HV5. This analysis emphasises that the prediction models are relatively accurate compared to the average response values. However, for a more comprehensive interpretation of the accuracy of the models, it is important to consider the ratio of the S_e error to the average value.

Mean Absolute Percentage Error - MAPE is a measure of prediction error used to evaluate the accuracy of forecasting models. It is often used because it is easy to interpret. The percentage error is easy to understand as it indicates the average percentage by which the predictions deviate from the actual values. The *MAPE* parameter was calculated for all values measured under the selected precipitation hardening conditions and then compared with the model's predictions for these points. The model shows a deviation of 2.9 % for tensile strength, 2.1 % for Charpy impact toughness, and 2.7 % for Vickers hardness.

The equations for tensile strength, Vickers hardness, and Charpy impact toughness collectively illustrate the complex dependencies of the aging conditions (T [°C] and t [h]) on the measured mechanical properties. The final mathematical model calculates the coefficients for the relationship between the predicted variables and the response variables and estimates: the Vickers hardness – *HV* [HV5] by Eq. (4), the Charpy impact toughness - *Charpy* [J] by Eq. (5) and the tensile strength - R_m [MPa] by Eq. (6).

$$HV = 307.708 + 0,475 \cdot T - 2502,374 \cdot t + 10,490 \cdot t \cdot T - 0,011 \cdot t \cdot T^2 - 0,801 \cdot t^3 \quad (4)$$

$$Charpy = 45.553 - 0.08997 \cdot T - 6.938 \cdot t + 1.40 \cdot 10^{-2} \cdot t \cdot T \quad (5)$$

$$Rm = 956.460 - 1.467 \cdot T + 139.523 \cdot t - 5.740 \cdot 10^{-3} \cdot T^2 - 2.005 \cdot t^3 \quad (6)$$

Table 3
Goodness of fit criteria.

	Tensile strength	Charpy impact toughness	Vickers hardness
R^2 [/]	0972	0934	0952
S_e	48,15 MPa	2133 J	23,86 HV5
MAPE [%]	2,9	2,1	2,7

Fig. 10 shows a graphical representation of the mathematical model equations. The mathematical models exhibit greater accuracy in regions close to the measurements obtained, which means that larger deviations are to be expected near the edges of the region of interest. In the following, the predictive mathematical models are evaluated using key metrics and visualisations.

The contour diagram in Fig. 10a illustrates the modelled Vickers hardness response as a function of the aging conditions. It shows an increasing hardness trend that exceeds 670 HV5. The region of maximum hardness is within the aging time interval of 3.2–5.7 h and at temperatures above 475 °C. The influence of the aging time on the response variable is smaller than the influence of the temperature. This is supported by the model Eq. (4), in which the presence of a negative linear term, -2502.374•*t*, suppresses the increase in Vickers hardness as the time variable increases. This effect becomes more significant at longer times and counteracts the other terms in the model that contribute positively to the response. The term with the largest positive contribution to the response is the interaction term, +10.490•*t*•*T*, followed by the linear term, +0.475•*T*. These terms drive the response toward the region of maximum hardness and dominate over the negative contributions of the other terms. The statistical parameters, $R^2 = 0.952$ and *MAPE* = 2.7 %, indicate a good fit of the model to the actual system behaviour. The model can be used as a reliable tool for predicting the system response.

Fig. 10b illustrates the trend of the Charpy impact toughness model. The highest toughness was observed in the material after solution annealing, which decreases during precipitation hardening, which is consistent with the diagram that suggest the highest toughness values at low aging times and temperatures and the lowest toughness in the region of highest hardness. An increase in Charpy notched impact strength can be seen towards the edges of the region of interest. The discrepancy to the measured values is most significant in this region. The model indicates a characteristic baseline-dominated system defined by a dominant constant component of Eq. (5). The response variable is largely influenced by this constant, while the predictors show a limited, weakly non-linear response and cause only minor deviations from the constant. This is also confirmed by the model equation, in which the small value of the interaction term $+1.40 \bullet 10^{-2} \bullet t \bullet T$ indicates only a slight curvature of the response surface. The predicted values are highly concentrated around the mean value of the system of 11.5 J, which is in the centre of the contour diagram. The statistical parameters, $R^2 = 0.934$ and *MAPE* = 2.1 %, show good accuracy as the model successfully captures most of the variance caused by the constant component. The model is highly accurate for the majority of the data as it effectively captures the average value of the system. However, it is less effectively for extreme values (either low or high) that occur at the edges of the region of interest in the contour plot.

The contour diagram in Fig. 10c illustrates the modelled tensile strength as a function of temperature and aging time. The model predicts the lowest tensile strength at short aging time and low temperature according by Eq. (6). The tensile strength increasing with temperature and aging time, as can be seen from the contour plot. The model predicts the highest values at the edge of the region of interest, at the highest temperatures, at over 2100 MPa. The contours in the graph are almost parallel, indicating a predominantly linear trend of increasing tensile strength towards the maximum value. This is also supported by the small value of the cubic term in the model Eq. (6), -2.005•t^3, which indicates a minimal contribution to the system response and only acts as a slight correction to the parallel contour lines. The combination of the metrics from Table 3 together with the analysis of the model equation and the contour plot confirms that the model reliably describes the system. The minimum error (*MAPE* = 2.9 %) further emphasises its utility. The model is therefore suitable for prediction and optimisation of the response variables over a wide range of input parameters.

The manufacturer of the filler and the base material specify a heat treatment temperature of 480 °C for 4 h (ASM International, 2009;

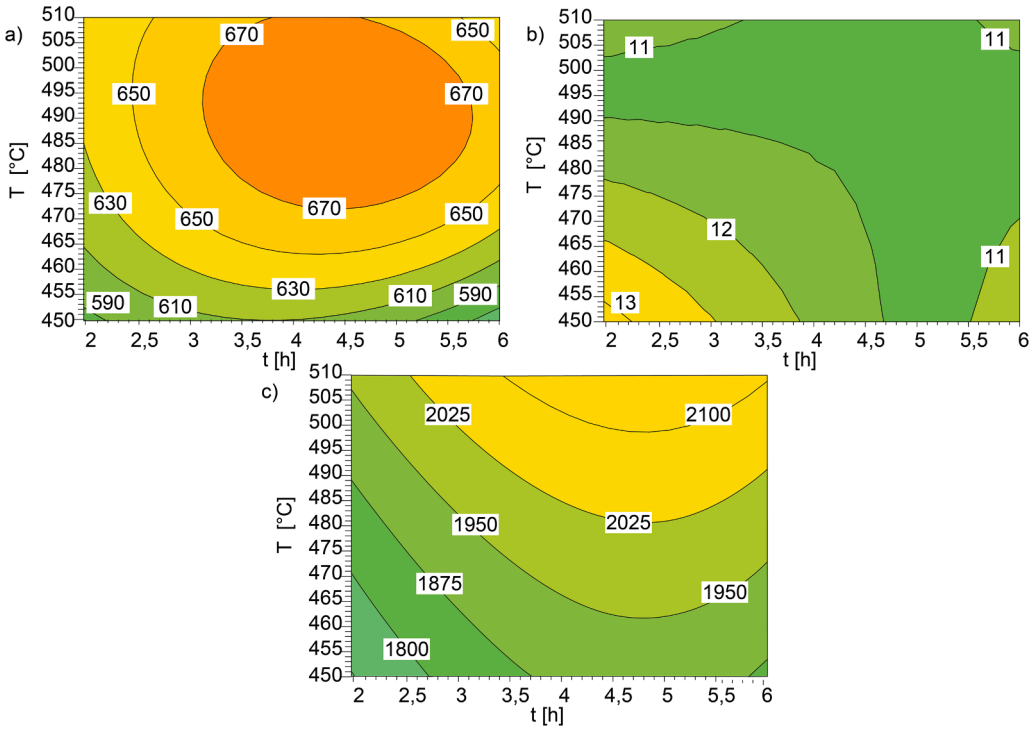

Fig. 10. Contour graph models of predicted: a) Vickers hardness [HV5], b) Charpy impact toughness [J] and c) tensile strength [MPa].

Schweissmaterialien GmbH, 2024). The diagrams in Fig. 9 show that the highest hardness values are achieved in this range. In industry, however, it is crucial to achieve a balance between the various mechanical properties, so optimisation based on hardness alone is generally not sufficient. In the tooling industry, for example, where maraging steels are often used, the mechanical hardness requirements for plastic injection moulding processes are between 545 and 670 HV, while die-casting applications require hardness between 437 and 508 HV (Klobčar et al., 2008). For plastic injection moulding processes, optimised heat treatment conditions in the temperature range of 470–510 °C with ageing times of >5 h could be proposed on the basis of experimental results. For desired hardness, the one can select the heat treatment that has beneficial Charpy toughness and tensile strength.

Conclusions

The research presents a fundamental characterisation and a multi-objective optimization of the heat treatment of maraging steel deposited with DED-ARC using GMAW technology. The developed heat treatment of maraging steel deposited with DED-ARC enables mechanical properties comparable to those of forged material. Based on the research results, we conclude that:

1) A high-quality DED-ARC process is essential to achieve the desired deposition without metallurgical deposition defects such as porosities, lack of fusion and cracks. A high energy input of 200 A and a travelling speed of 3 mm/s in combination with high interpass temperatures of 250 °C ensure proper material fusion during deposition. Each layer should be cleaned with a stainless-steel wire brush before the next layer is deposited.
2) A characteristic microstructure in as-built condition has very long crystalline grains and some segregation zones oriented towards the heat sink, and various metallic inclusions (e.g. spherical TiAlO and TiMoC) were obtained in the microstructure.
3) The SA1 solution annealing procedure (920 °C, 1 h) proved inadequate, as it did not completely eliminate the inhomogeneity of the microstructure. Precipitation hardening has no influence on homogeneity. The SA1 + Peak aged Charpy fracture revealed the presence of cleavage areas, indicating a trans-granular fracture Charpy impact toughness of 5 J. This contrasts with the SA2 + Peak aged sample (SA2 + PH7), which had a Charpy impact toughness of 11 J and exhibited an inter-granular brittle fracture. This indicates that solution annealing significantly influences the post-precipitation hardening conditions and the final material properties.
4) SA2 solution annealing procedure (1150 °C, 1 h; 595 °C, 1 h; 850 °C, 1 h) resulted in a fine-grained and uniform microstructure, which positively influences the mechanical properties. Solution annealing plays a decisive role in reducing inhomogeneity and segregation and therefore has a significant influence on the final mechanical properties.
5) Under-aged conditions have less pronounced precipitation. They have a lower hardness of 612–680 HV5 and a ultimate tensile strength of 1777–2079 MPa with an elongation of 1.6–4.2 % and a Charpy impact toughness of 10–13 J.
6) Under Peak-aged conditions, the material achieved the highest Vickers hardness of 632–709 HV5, an average ultimate tensile strength of 1947–2019 MPa and an elongation of 2–2.9 %, while exhibiting the lowest Charpy impact toughness levels of 11–12 J.
7) In Over-aged conditions exhibits the highest ultimate tensile strength is 2012–2200 MPa and an elongation of 1.9–3.1 % as well as a Charpy impact toughness of 9–14 J, while the Vickers hardness is 633–689 HV5. A lower Charpy impact toughness is achieved with longer precipitation hardening times, during which the microstructure is highly overaged.
8) The regression models developed for the prediction of tensile strength, Charpy impact toughness, and Vickers hardness based on temperature and time of precipitation hardening are a suitable tool for predicting and optimising of the response variables over a wide range of input parameters. A general purpose of the optimal post-processing heat treatment for plastic injection moulding would be 470–510 °C with a precipitation hardening time > 5 h, allowing an ultimate tensile strength of 2000–2100 MPa, Vickers hardness of < 670 HV, and Charpy impact toughness >11 J.

CRediT authorship contribution statement

Maja Lindič: Writing – original draft, Visualization, Software, Investigation, Formal analysis, Data curation. **Damjan Klobčar:** Writing – review & editing, Validation, Supervision, Resources, Funding acquisition, Conceptualization. **Aleš Nagode:** Writing – review & editing, Validation, Investigation, Conceptualization. **Nikolaj Mole:** Writing – review & editing, Supervision. **Borut Žužek:** Writing – review & editing, Investigation. **Tomaž Vuherer:** Writing – review & editing, Validation, Investigation.

Declaration of competing interest

The authors declare the following financial interests/personal relationships which may be considered as potential competing interests:

Damjan Klobcar reports financial support was provided by Slovenian Research and Innovation Agency. If there are other authors, they declare that they have no known competing financial interests or personal relationships that could have appeared to influence the work reported in this paper.

Acknowledgments

This research was funded by Slovenian Research Agency under grant number P2-0270, and bilateral project Weave N2-0328. This work was supported by the Slovenian Research Agency, under grant number BI-BA/24-25-034 and BI-TR/22-24-08. The research was also partly supported by EU ERASMUS+ Strategic Partnership Key Action 2, number: 2024-1-RO01-KA220-HED-000244949 (SMARTIE) and 2023-1-RO01-KA220-HED-000158031 (ANGIE).

Data availability

Data will be made available on request.

References

ASM Handbook, Volume 4: Heat treating, 9. print, 2009. ASM International, Materials Park, Ohio.

Adzor, S.A., Nwaeju, C.C., Edoziuno, F.O., 2022. Optimization of tensile strength for heat treated micro-alloyed steel weldment. Mater. Today: Proc. 56, 1956–1963. https://doi.org/10.1016/j.matpr.2021.11.282.

Armstrong, J.S., Collopy, F., 1992. Error measures for generalizing about forecasting methods: empirical comparisons. Int. J. Forecast. 69–80. https://doi.org/10.1016/0169-2070(92)90008-W n.d.

Carvalho, L.G.D., Plaut, R.L., Lima, N.B.D., Padilha, A.F., 2019. Kinetics of martensite reversion to Austenite during overaging in a Maraging 350 steel. ISIJ Int. 59, 1119–1127. https://doi.org/10.2355/isijinternational.ISIJINT-2018-610.

Chen, M., Liu, X., Zhao, F., Xiao, X., Xie, J., 2024. Significantly enhancing the ductility of high-strength Cu-15Ni-8Sn alloy via an optimized combined process of deformation and heat treatment. Mater. Sci. Eng. A 914, 147154. https://doi.org/10.1016/j.msea.2024.147154.

Frihat, M.H., 2015. Effect of heat treatment parameters on the mechanical and microstructure properties of low-alloy steel. JSEMAT 05, 214–227. https://doi.org/10.4236/jsemat.2015.54023.

Guo, L., Zhang, L., Andersson, J., Ojo, O., 2022. Additive manufacturing of 18% nickel maraging steels: defect, structure and mechanical properties: a review. J. Mater. Sci. Technol. 120, 227–252. https://doi.org/10.1016/j.jmst.2021.10.056.

Hashmi, S. (Ed.), 2017. Comprehensive Materials Finishing. Elsevier, Amsterdam Boston Heidelberg.

Jägle, E.A., Choi, P.-P., Van Humbeeck, J., Raabe, D., 2014. Precipitation and austenite reversion behavior of a maraging steel produced by selective laser melting. J. Mater. Res. 29, 2072–2079. https://doi.org/10.1557/jmr.2014.204.

Jorge, L.D.J., Cândido, V.S., Silva, A.C.R.D., Garcia Filho, F.D.C., Pereira, A.C., Luz, F.S. D., Monteiro, S.N., 2018. Mechanical properties and microstructure of SMAW welded and thermically treated HSLA-80 steel. J. Mater. Res. Technol. 7, 598–605. https://doi.org/10.1016/j.jmrt.2018.08.007.

Kage, M., Miller, K.J., Smith, R.A., 1992. Fatigue crack initiation and propagation in a low-carbon steel of two different grain sizes. Fatigue Fract. Eng. Mat. Struct. 15, 763–774. https://doi.org/10.1111/j.1460-2695.1992.tb00055.x.

Klobčar, D., Tušek, J., Taljat, B., Kosec, L., Muhič, M., 2008. Suitability of maraging steel weld cladding for repair of die casting tooling: part II: influence of ageing during aluminium alloy die casting on maraging steel weld microstructure, mechanical properties and crack growth. Int. J. Mater. Res. 99, 1006–1014. https://doi.org/10.3139/146.101733.

Kozamernik, N., Bračun, D., Klobčar, D., 2020. WAAM system with interpass temperature control and forced cooling for near-net-shape printing of small metal components. Int. J. Adv. Manuf. Technol. 110, 1955–1968. https://doi.org/10.1007/s00170-020-05958-8.

Lang, F.H., Kenyon, N., 2021. Welding of Maraging Steels - A Practical Guide to the Use of Nickel-Containing Alloys No 584. The Nickel Institute, pp. 0–40 n.d.

Liu, G., Su, J., Wang, A., Yang, Z., Ding, Y., Ning, J., Gao, Q., 2023. A novel Fe–Cr–Ni–Co–Mo maraging stainless steel with enhanced strength and cryogenic toughness: role of austenite with core-shell structures. Mater. Sci. Eng. A 863, 144537. https://doi.org/10.1016/j.msea.2022.144537.

Liu, Y., Zhu, J., Cao, Y., 2017. Modeling effects of alloying elements and heat treatment parameters on mechanical properties of hot die steel with back-propagation artificial neural network. J. Iron Steel Res. Int. 24, 1254–1260. https://doi.org/10.1016/S1006-706X(18)30025-6.

Murthy, C.V.S., Gopala Krishna, A., Reddy, G.M., 2019. Microstructure and mechanical properties of similar and dissimilar metal gas tungsten constricted arc welds: maraging steel to 13-8 Mo stainless steel. Def. Technol. 15, 111–121. https://doi.org/10.1016/j.dt.2018.04.005.

Nunes, M.M., Silva, E.M.D., Renzetti, R.A., Brito, T.G., 2018. Analysis of quenching parameters in AISI 4340 steel by using design of experiments. Mat. Res. 22. https://doi.org/10.1590/1980-5373-mr-2018-0315.

Powar, A., Date, P., 2015. Modeling of microstructure and mechanical properties of heat treated components by using artificial neural network. Mater. Sci. Eng. A 628, 89–97. https://doi.org/10.1016/j.msea.2015.01.044.

Qu, J., Cherkaoui, M., 2006. Fundamentals of Micromechanics of Solids, 1st ed. Wiley. https://doi.org/10.1002/9780470117835.

Ray, P.K., Ganguly, R.I., Panda, A.K., 2003. Optimization of mechanical properties of an HSLA-100 steel through control of heat treatment variables. Mater. Sci. Eng. A 346, 122–131. https://doi.org/10.1016/S0921-5093(02)00526-9.

Razavi, S.A., Ashrafizadeh, F., Fooladi, S., 2016. Prediction of age hardening parameters for 17-4PH stainless steel by artificial neural network and genetic algorithm. Mater. Sci. Eng. A 675, 147–152. https://doi.org/10.1016/j.msea.2016.08.049.

Ščetinec, A., Klobčar, D., Nagode, A., Vuherer, T., Bračun, D., Trdan, U., 2023. Optimisation of precipitation hardening for 15-5 PH martensitic stainless steel produced by wire arc directed energy deposition. Sci. Technol. Weld. Join. 28, 558–568. https://doi.org/10.1080/13621718.2023.2202979.

Schweissmaterialien GmbH, 2024. Capilla - Part catalogue; 4. Welding Consumables For Welding of Tool Steels. Schweissmaterialien GmbH, Leopoldshoehe, Germany. https://www.capilla-gmbh.com/wp-content/uploads/Katalog_04_en.pdf.

Song, R.G., Zhang, Q.Z., 2001. Heat treatment technique optimization for 7175 aluminum alloy by an artifcial neural network and a genetic algorithm. J. Mater. Process. Technol. 2001, 84–88. https://doi.org/10.1016/S0924-0136(01)01114-1.

voestalpine BÖHLER Edelstahl GmbH & Co KG, BÖHLER - W720VMR hot Work Tool Steel, voestalpine BÖHLER Edelstahl GmbH & Co KG, Kapfenberg, Austria, n.d. https://www.bohler-edelstahl.com/app/uploads/sites/248/productdb/api/w720-vmr_en_gb.pdf.

N.A. Weiss, Introductory STATISTICS, 9th ed., Pearson Education, n.d.

Wember, T.D., 2012. Design of Experiment (DoE): Systematic and Efficient Development of Product and Processes and Empirical Model Building Based on Statistical Principles. https://books.google.si/books?id=Nj96MwEACAA.

Xu, X., Ding, J., Ganguly, S., Diao, C., Williams, S., 2019a. Preliminary investigation of building strategies of maraging steel bulk material using wire + arc additive manufacture. J. Mater. Eng. Perform. 28, 594–600. https://doi.org/10.1007/s11665-018-3521-5.

Xu, X., Ganguly, S., Ding, J., Dirisu, P., Martina, F., Liu, X., Williams, S.W., 2019b. Improving mechanical properties of wire plus arc additively manufactured maraging steel through plastic deformation enhanced aging response. Mater. Sci. Eng. A 747, 111–118. https://doi.org/10.1016/j.msea.2018.12.114.

Xu, X., Ganguly, S., Ding, J., Guo, S., Williams, S., Martina, F., 2018. Microstructural evolution and mechanical properties of maraging steel produced by wire + arc additive manufacture process. Mater. Charact. 143, 152–162. https://doi.org/10.1016/j.matchar.2017.12.002.

Xu, Y., Mishra, B., Narra, S.P., 2022. Experimental investigation of in-situ microstructural transformations in wire arc additively manufactured maraging 250-grade steel. Mater. Charact. 190, 112065. https://doi.org/10.1016/j.matchar.2022.112065.

Yang, G., Deng, F., Zhou, S., Wu, B., Qin, L., 2021. Microstructure and mechanical properties of a novel Cu-reinforced maraging steel for wire arc additive manufacturing. Mater. Sci. Eng. A 825, 141894. https://doi.org/10.1016/j.msea.2021.141894.

Yang, G., Deng, F., Zhou, S., Wu, B., Qin, L., Zheng, J., 2022. Influence of shielding gas nitrogen content on the microstructure and mechanical properties of Cu-reinforced maraging steel fabricated by wire arc additive manufacturing. Mater. Sci. Eng. A 832, 142463. https://doi.org/10.1016/j.msea.2021.142463.

Zhang, Y., Yang, L., Chen, T., Zhang, W., Huang, X., Dai, J., 2017. Investigation on the optimized heat treatment procedure for laser fabricated IN718 alloy. Opt. Laser Technol. 97, 172–179. https://doi.org/10.1016/j.optlastec.2017.06.027.